AGU PUBLICATIONS

Geophysical Research Letters

RESEARCH LETTER
10.1002/2014GL061686

Key Points:
- A finite-fault rupture model is found to match global seismic and near-field tsunami observations
- Far-field tsunami surges around the Hawaiian Islands provide independent validation
- Detailed slip distribution influences tsunami waves even for a compact source

Supporting Information:
- Readme
- Figure S1
- Figure S2
- Figure S3

Correspondence to:
K. F. Cheung,
cheung@hawaii.edu

Citation:
Bai, Y., K. F. Cheung, Y. Yamazaki, T. Lay, and L. Ye (2014), Tsunami surges around the Hawaiian Islands from the 1 April 2014 North Chile M_w 8.1 earthquake, *Geophys. Res. Lett.*, *41*, 8512–8521, doi:10.1002/2014GL061686.

Received 27 AUG 2014
Accepted 30 OCT 2014
Accepted article online 4 NOV 2014
Published online 9 DEC 2014

Tsunami surges around the Hawaiian Islands from the 1 April 2014 North Chile M_w 8.1 earthquake

Yefei Bai[1], Kwok Fai Cheung[1], Yoshiki Yamazaki[1], Thorne Lay[2], and Lingling Ye[2]

[1]Department of Ocean and Resources Engineering, University of Hawaii at Manoa, Honolulu, Hawaii, USA, [2]Department of Earth and Planetary Sciences, University of California Santa Cruz, Santa Cruz, California, USA

Abstract The 1 April 2014 Iquique M_w 8.1 earthquake ruptured a segment of the megathrust fault offshore of northern Chile and generated a moderate-size tsunami across the Pacific. Tide gauges in Hawaii recorded over 1 m of wave height despite the long distance from the source and position away from the main radiated energy lobe. Inversion of global teleseismic body waves combined with forward modeling of the tsunami at four near-field DART stations arrives iteratively at a self-consistent finite-fault model with very compact dimensions. The slip distribution produces a NNE-SSW trending seafloor uplift patch that enhances the tsunami directionality in the WNW, resulting in good matches to observed DART and tide gauge records around the Hawaiian Islands. The relatively large waves at selected locations in Hawaii can be attributed to a combination of the spatial slip distribution and the resulting short-period waves that triggered localized resonance over the insular shelves. This event highlights the importance of characterizing detailed slip distributions in analysis or forecasting of tsunamis even for a compact source.

1. Introduction

Tsunami waves from submarine earthquakes propagate at much lower speeds than rupture expansion and seismic waves, and their amplitude and period are intrinsically sensitive to the coseismic seafloor deformation. These attributes are commonly exploited in solving for earthquake rupture properties by tsunami wave inversion [e.g., *Satake*, 1987, 1989; *Saito et al.*, 2011; *Satake et al.*, 2013; *An et al.*, 2014], joint inversion of tsunami and geodetic data [e.g., *Satake*, 1993; *Romano et al.*, 2010, 2012, 2014], iterative forward modeling with seismic data inversion [e.g., *Lay et al.*, 2011a, 2011b, 2013a, 2013b; *Yamazaki et al.*, 2011b, 2013; *Yue et al.*, 2014a], or joint inversion of multiple data sets [e.g., *Lorito et al.*, 2011; *Yokota et al.*, 2011; *Lay et al.*, 2014; *Yue et al.*, 2014b; *Bletery et al.*, 2014]. The robust relationship between tsunami signals and earthquake faulting patterns has also enabled development of real-time forecast guidance by the NOAA Center for Tsunami Research (NCTR) through inversion of DART measurements [*Wei et al.*, 2003, 2008; *Titov et al.*, 2005].

On 1 April 2014, a shallow interplate thrusting M_w 8.1 earthquake struck in the subduction zone offshore of Iquique, northern Chile at 19.610°S, 70.769°W and 23:46:47 UTC [http://comcat.cr.usgs.gov/earthquakes/eventpage/usc000nzvd#summary]. The tsunami swept past the Hawaiian Islands 13.5 h later, and the tide gauge records show 0.62 and 0.50 m of maximum wave amplitude at Hilo and Kahului but only 0.05 and 0.06 m at Honolulu and Nawiliwili (see Figure 1 for location map). Inversion using DART 32401 and 32402 by NCTR shows a 5 min early arrival at DART 32402 south of the source and underestimates the initial peaks at Hawaii tide gauges [http://nctr.pmel.noaa.gov/chile20140401/]. *Lay et al.* [2014], *Ruiz et al.* [2014], *Hayes et al.* [2014], and *Schurr et al.* [2014] inverted teleseismic body waves for the slip distribution of the main shock. In particular, *Lay et al.* [2014] constrained their seismic fault model parameterization based on an initial low-resolution joint inversion including DART 32401, 32402, and 32412 recordings. *An et al.* [2014] inverted the same DART observations, but the forward modeling results show discrepancies in arrival time and amplitude of the initial wave at near-field tide gauges. The main shock slip in these published models is concentrated over a region spanning less than 100 km along strike and less than 50 km along dip southeast of the hypocenter. These compact sources, however, vary in orientation and distribution in contrast with the uniform slip assumed for the NCTR subfaults of comparable size.

The compact source and the varying results published so far suggest that the 2014 Iquique, Chile earthquake is a good case study to examine effects of subtle fault features on the near- and far-field tsunami waves. We

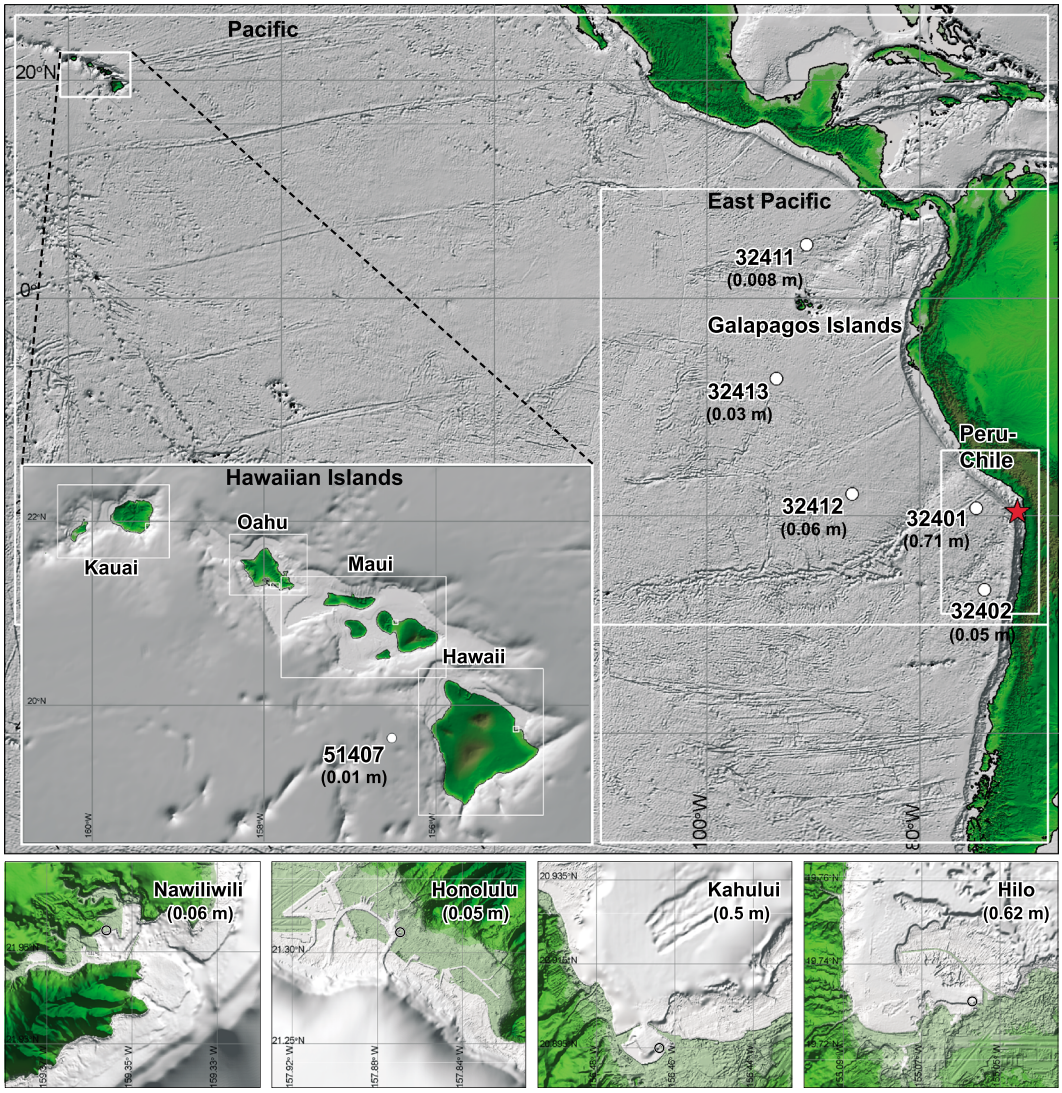

Figure 1. Location maps and computational grid systems for modeling of the tsunami generated by the 1 April 2014 Iquique, Chile M_w 8.1 earthquake. White circles and adjacent labels denote DART stations, and black open circles indicate tide gauge locations. Maximum recorded wave amplitudes are indicated in parentheses adjacent to the stations.

take a different approach from the previous studies of the event by inverting the seismic waves and forward modeling the near-field tsunami records to iteratively derive a self-consistent finite-fault model that can match both data sets. Earthquake source models optimized with offshore tsunami observations have provided valuable input to detailed investigations of coastal and harbor resonance for hazard assessments [e.g., *Yamazaki et al.,* 2012; *Cheung et al.*, 2013]. A self-consistent fault model allows examination of whether a more detailed source representation can explain the discrepancies observed in the near field and improve on the prediction of the tsunami signals around the Hawaiian Islands. While the NCTR is exploring the use of joint inversion to provide a new generation of tsunami forecast guidance [*Wei et al.*, 2014], we investigate possible improvements in tsunami forecast models using more complex faulting patterns.

2. Methodology

The source model optimization for the 2014 Iquique, Chile earthquake combines finite-fault inversion of seismic waves with forward tsunami modeling for comparison with near-field DART records that in turn provides the basis for iterative adjustment of poorly constrained source parameters [*Yamazaki et al.*, 2011b;

and *Lay et al.,* 2013a, 2013b]. Figure 1 shows the locations of the epicenter and the water-level stations considered in this study. We utilize global broadband recordings of seismic ground motions as well as water-level measurements from DART 32401, 32402, 32412, and 32413 spanning a 120° azimuth range from the epicenter to derive the earthquake source. Inclusion of DART 32413 in the forward modeling, in addition to the three considered in *Lay et al.* [2014] and *An et al.* [2014], provides improved constraints on the fault model that accounts for the sidelobe energy toward the North Pacific.

To constrain the overall faulting mechanism, we first applied the W-phase point-source inversion method of *Kanamori and Rivera* [2008] to 160 long-period ground motion recordings from 112 global seismic stations with stable signals in the period range 200 to 1000 s. The long-period moment tensor is almost a pure double-couple with strike 348.7°, dip 14°, and rake 90.7°, and seismic moment of 2.0×10^{21} Nm. The strike is parallel to the adjacent trench so it reliably represents the local tectonics. The dip, which trades off inversely with seismic moment due to the use of long-period surface waves, is not tightly constrained [e.g., *Kanamori and Given*, 1981]. We then performed linear least squares finite-fault inversion using 52 teleseismic *P* wave and 49 *SH*-wave ground displacements band-pass filtered in the period range 0.9 to 200 s [*Lay et al.*, 2014]. For a given dip angle, the total fault model dimensions and geometry, the rupture front expansion velocity, subfault dimensions, smoothing parameters, and subfault source time functions are varied over plausible ranges using a multi-time window, linear inversion routine adapted from *Kikuchi and Kanamori* [1991].

For each finite-fault model that fits 80–90% of the teleseismic signal power, we forward-modeled the sea-surface elevations at the four DARTs. The shock-capturing dispersive wave code NEOWAVE of *Yamazaki et al.* [2009, 2011a] is used to calculate the tsunami from its generation by the earthquake rupture to propagation across the ocean. The planar fault model of *Okada* [1985] defines the kinematic seafloor deformation from the time-varying subfault motions and provides the seafloor displacement and velocity for the tsunami modeling. The staggered finite difference code builds on the nonlinear shallow-water equations with a vertical velocity term to account for weakly dispersive waves and a momentum conservation scheme to describe bore formation. The vertical velocity term also accounts for the time sequence of seafloor uplift and subsidence and facilitates dispersion of the seafloor excitation over the water column during tsunami generation. The method of *Tanioka and Satake* [1996] approximates the vertical motion resulting from the seafloor horizontal displacement on a slope.

We explore the finite-fault parameter space, varying the rupture velocity and grid dimensions and spacing, to achieve optimal agreement with the seismic and tsunami observations. The preferred source model then defines the input for computation of the sea-surface elevations at DART 32411 and 51407 as well as four tide gauges around the Hawaiian Islands for validation. The modeling effort involves two systems of two-way nested grids outlined in Figure 1. The iterative modeling of the seismic source utilizes a 30 arcsec (~900 m) grid to resolve the Peru and north Chile coasts and a 2 arcmin (~3600 m) grid for radiation of the wave energy into the eastern Pacific. The far-field modeling requires four levels of nested grids with 2 arcmin (~3600 m) for the Pacific, 24 arcsec (~720 m) around the Hawaiian Islands, and 3 arcsec (~90 m) around each island or island group for transition to 0.3 arcsec (~9 m) at the tide gauge locations. The digital elevation model consists of the GEBCO data set at 30 arcsec (~900 m) across the Pacific Ocean and multi-beam and LiDAR survey data at 50 m and 1–3 m resolution around the Hawaiian Islands. A Manning number of 0.035 describes the subgrid roughness of the volcanic and reef substrate in Hawaii [*Bretschneider et al.*, 1986].

3. The Earthquake and Tsunami Models

Figure 2 displays the preferred slip model and the resulting seafloor deformation. The final parameterization includes eight subfaults along strike and six along dip with 15 km spacing. The preferred subfault source time functions involve four 2.5 s risetime triangles with 2.5 s time shifts between them, giving a maximum source duration of 12.5 s. We assumed a hypocentral depth of 22 km, held the strike fixed at the W-phase solution, and increased the dip to 18° to better match the slab dip near the large-slip region [e.g., *Hayes et al.*, 2012]. The model is slightly rotated from the global Centroid-Moment Tensor (gCMT) strike adopted by *Lay et al.* [2014] and tracks more closely the curvature of the trench similar to the NCTR subfaults. The primary slip patch and the resulting seafloor uplift feature a NNE-SSW alignment. The very concentrated slip distribution is compatible with geodetic inversions reported by *Schurr et al.* [2014]. The seismic moment of 1.3×10^{21} Nm is reduced from the W-phase solution by the increased dip but, due to the different source velocity structure used, is somewhat

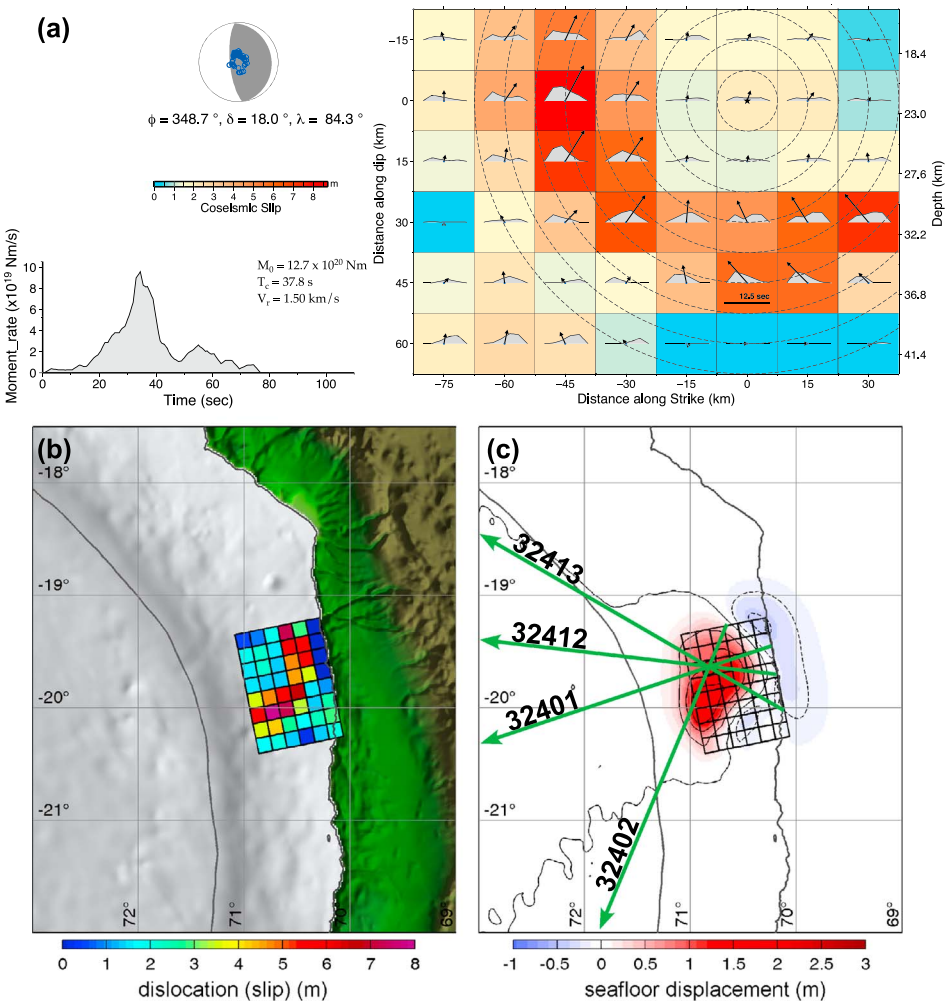

Figure 2. Preferred slip model and seafloor deformation from the iterative modeling procedure. (a) The overall moment rate function over a 75 s duration is shown at the left, with most of the moment concentrated between 20 and 45 s after the onset. The average focal mechanism is shown above with the locations of *P* wave sampling indicated in blue. The slip distribution is shown on the right for the 8 × 6 grid with 15 km spacing. The dashed circles are 5 s increments of rupture expansion. The color scale denotes the cumulative slip and the vectors indicate the average rake and slip in the fault plane. The subfault source time functions shown are solved at each grid node, with 4 lagged 2.5 s risetime triangles of varying moment and rake. This accounts for 84% of the teleseismic *P* and *SH* broadband displacement waveform power for the signals used in the inversion. Waveform fits are shown in supporting information Figure S1. (b) The rupture model is shown in geographic position relative to the trench (gray line). (c) The seafloor uplift produced by the model is displayed along with azimuthal lines toward the four near-field tsunami stations indicated by the bold numbers and used in the iterative procedure.

smaller than the gCMT value of 1.7×10^{21} Nm (for PREM) with the same dip. The precise source depth, dip, and seismic moment are not uniquely resolved, but the preferred model provides excellent agreement with the teleseismic records in Figure S1 of the supporting information.

The computed tsunami from the preferred model also provides excellent agreement with the records as shown in Figure 3. Matching the distinct initial waves from DART 32401, 32402, 32412, and 32413 plays a predominant role in constraining the slip within the confines of the kinematic rupture model. The source model dimensions were contracted somewhat relative to the already compact model in *Lay et al.* [2014], and the rupture velocity was reduced to 1.5 km/s in order to keep the spatial slip distribution sufficiently concentrated to match the pulse width at all four DART stations. The location of the slip relative to the hypocenter controls the absolute arrival times of the tsunami signals at the DART stations. This places the primary slip to the east and southeast from the hypocenter within the 15–35 s isochrones of the rupture

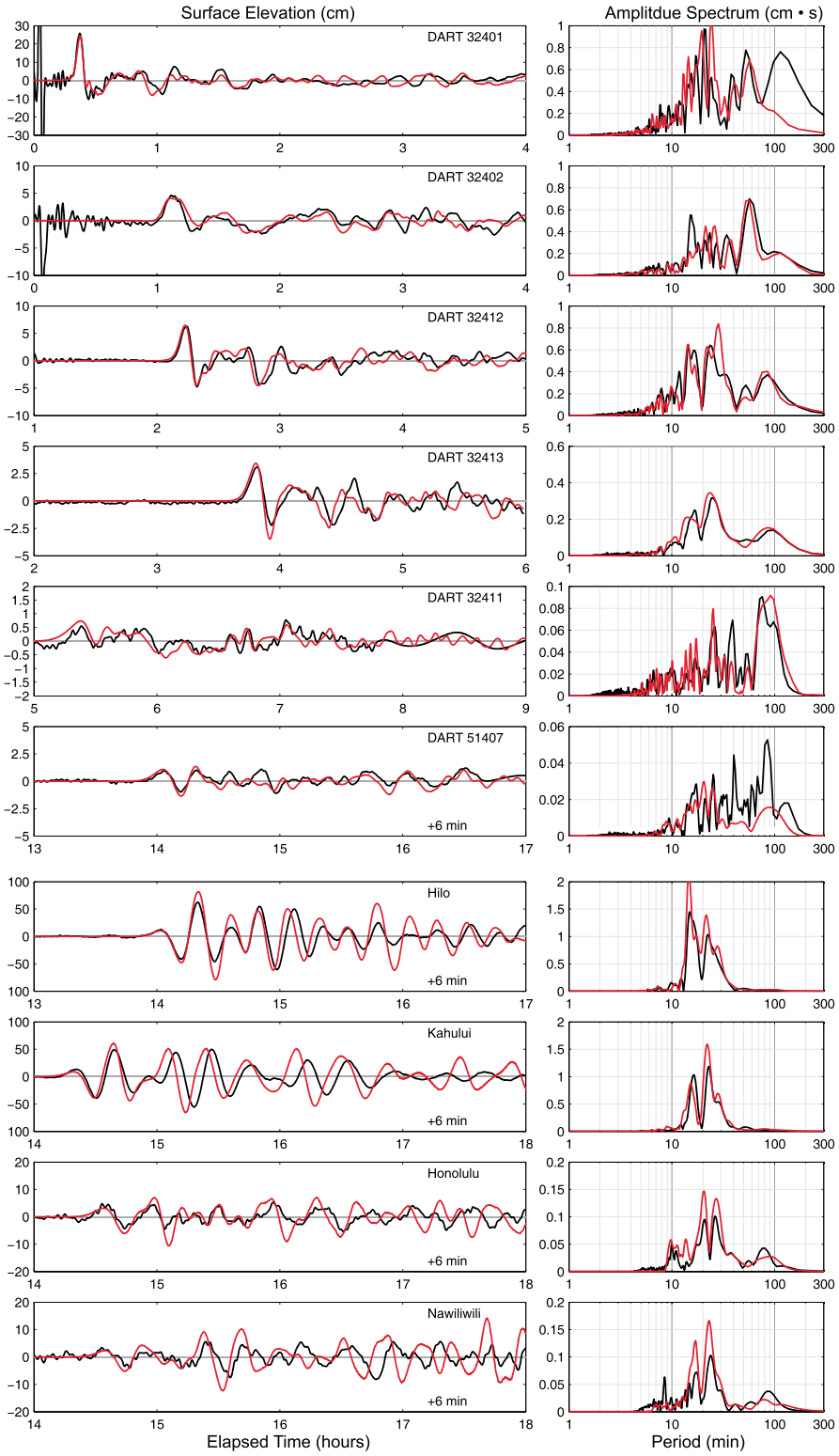

Figure 3. Comparison of detided records (black) and computed tsunami waveforms (red) at water-level stations. Near-field DART 32401, 32402, 32412, and 32413 are included in the forward modeling scheme. Precise matching of the amplitude and timing of the recorded tsunami signals is essential in constraining the slip distribution from the finite fault inversion. The computed waveforms at DART 51407 and the Hawaii tide gauges have been shifted by 6 min to account for early arrival of the computed tsunami. The agreement at DART 32411 and 51407 and the four tide gauges in Hawaii validates the preferred source model.

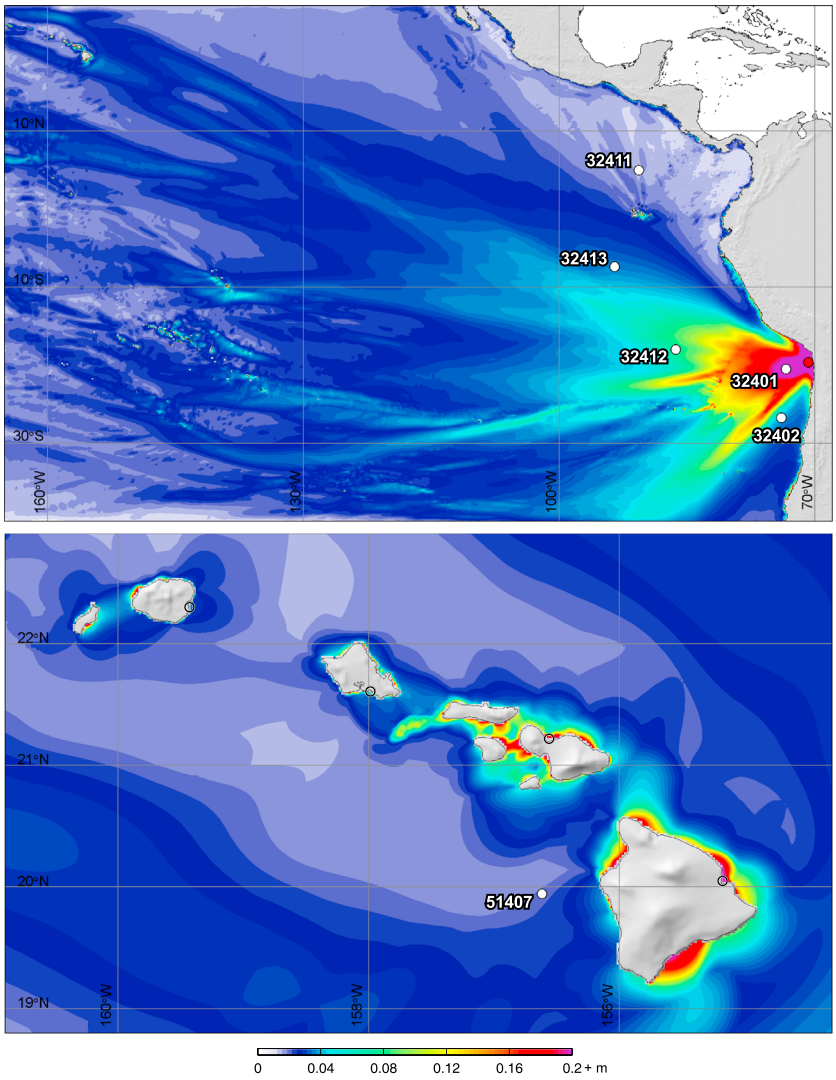

Figure 4. Computed maximum wave amplitude for the 2014 Iquique tsunami. The pattern across the Pacific shows an enhanced energy beam toward Hawaii. The short-period waves from the compact source excited localized resonance around the Hawaiian Islands. White circles and adjacent labels denote DART stations, and black open circles in the lower panel indicate tide gauge locations.

expansion as shown in Figure 2. No significant slip occurs updip of the hypocenter, as this would produce clear precursory arrivals that are not seen in the tsunami data. DART 32401 and 32412 recorded a wide second wave with double peaks that correspond to sequential arrivals of the rebound of the coseismic sea-surface pulse and its reflection from the Peru-Chile coast. Far away from the coast, DART 32413 recorded spectral peaks at 16 and 24 min associated with the principal rupture dimensions. The tsunami codas come from resonance along the Peru-Chile coasts with distinct periods between 35 and 129 min as identified by *Yamazaki and Cheung* [2011].

The records from DART 32411 and 51407 and the four Hawaii tide gauges, which were not considered in the iterative modeling procedure, allow independent validation of the source model. DART 32411 recorded small diffracted waves leeward of the Galapagos Islands. Despite the low resolution of 2 arcmin, the agreement between the computed and recorded tsunami waveforms is reasonably good. The computed time series around Hawaii have been shifted by 6 min to account for early arrival associated with the lack of earth elasticity and water density variation in the tsunami model [e.g., *Tsai et al.*, 2013; *Watada et al.*, 2014; *Allgeyer and Cummins*, 2014]. The computed and recorded data show good agreement of the initial waves as well as the overall wave height of the time series. The recorded signal at DART 51407 is weak with strong background

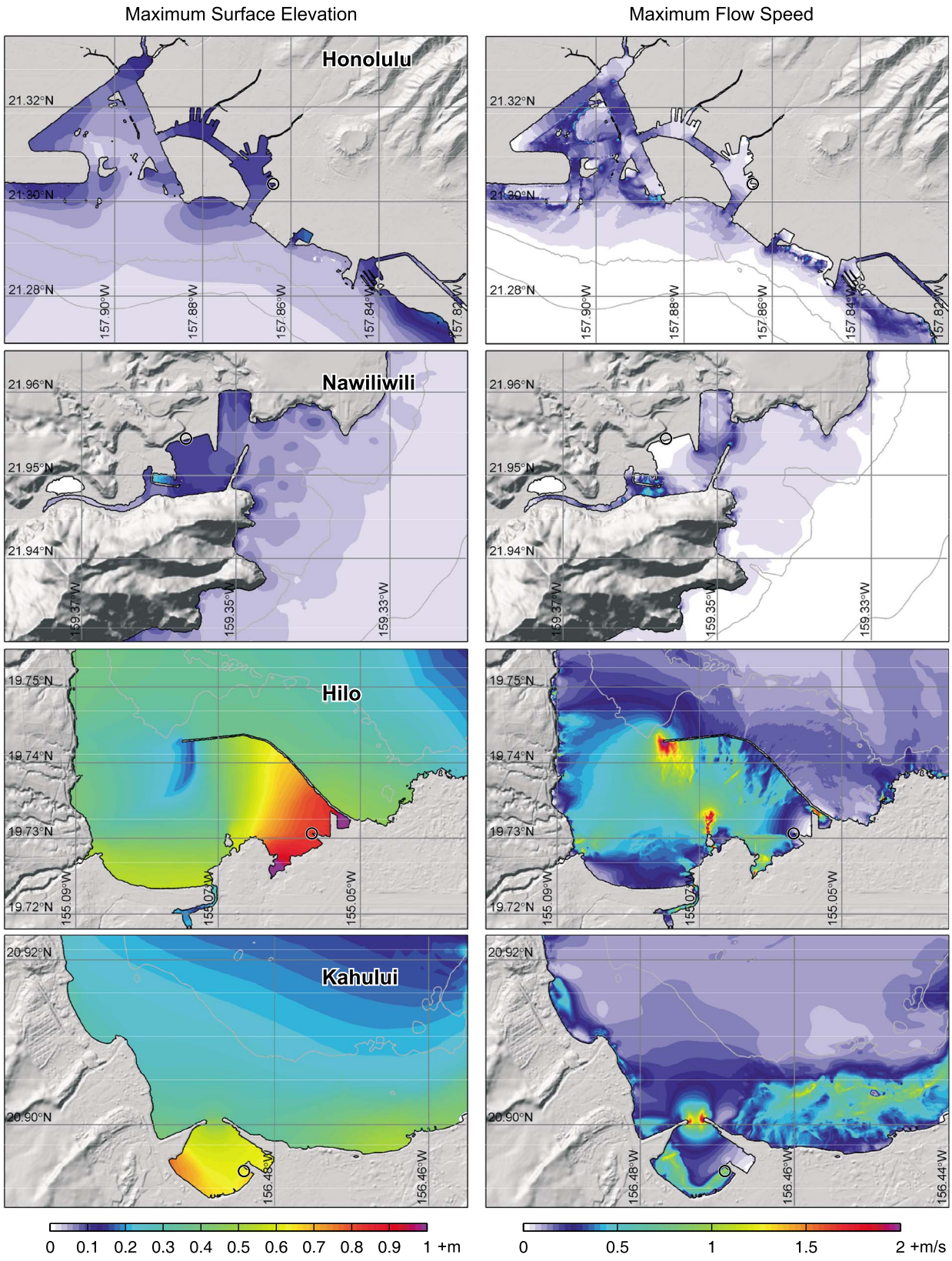

Figure 5. Computed maximum wave amplitude and flow speed at the four major commercial harbors of Hawaii. The tsunami wave periods coincide with natural periods of Hilo Bay and Kahului Bay. The resulting resonance oscillations have patterns similar to those generated by the 2011 Tohoku tsunami [*Cheung et al.*, 2013]. Black open circles indicate tide gauge locations.

oscillations but nevertheless has good agreement with the computed spectral peaks between 8 and 25 min period. The tsunami waves do not excite the inter-island oscillation modes with periods of 33 min and above [*Cheung et al.*, 2013]. The dominant 16 and 21 min components coincide with the shorter-period resonance modes of Hilo Bay and Kahului Bay to produce wave heights of over 1 m at the tide gauges. The model results also reproduce the order of magnitude smaller spectral peaks of the recorded signals at Honolulu and Nawiliwili.

Figure 4 plots the maximum wave amplitude across the Pacific and around the Hawaiian Islands. The distribution is typical of a compact source at which energy radiates over a wide azimuthal range. The 1.98 m of seafloor uplift generates a maximum wave amplitude of 1.90 m at the source due to dispersion. Refraction-diffraction of the radiated waves along seamount chains and submarine ridges generates the narrow energy beams to the west and southwest off the Chile coast. The NNE-SSW trending seafloor deformation produces radiated waves that attenuate at a slower rate in the WNW direction resulting in a wide, sustained energy beam toward Hawaii. The short-period waves associated with the compact source amplify in large embayments around Hawaii Island. The refracted-diffracted waves from Hawaii Island are trapped over the shallow insular shelf around Maui to produce the large amplitude waves observed at Kahului. These processes shelter Oahu and Kauai from the tsunami and together with the lack of interisland standing waves lead to relatively small waves at Honolulu and Nawiliwili as shown in Figure 5. The wave patterns in Hilo Bay and Kahului Bay are similar to those computed for the 2011 Tohoku tsunami by *Cheung et al.* [2013]. The resonance oscillations in Hilo Harbor have up to 1.1 m amplitude in the inner basin and 2.9 m/s flow speed adjacent to the breakwater that are comparable to 2.2 and 4.5 m/s computed for the much more energetic, 2011 Tohoku tsunami.

4. Discussion and Conclusions

The 1 April 2014 M_w 8.1 Iquique, Chile earthquake has received much attention due to its size and location in the northern third of a large seismic gap that last ruptured on 9 May 1877 with estimated seismic magnitude of 8.7–8.9 [*Comte and Pardo*, 1991; *Lay et al.*, 2014]. The earthquake had a distinctive foreshock sequence, which migrated spatially over several months prior to the main shock, and a large number of events following an M_w 6.7 foreshock on 16 March 2014 [e.g., *Brodsky and Lay*, 2014; *Bürgmann*, 2014; *Hayes et al.*, 2014; *Kato and Nakagawa*, 2014; *Ruiz et al.*, 2014; *Schurr et al.*, 2014; *Yagi et al.*, 2014]. Slow slip deformation may have driven this foreshock migration in a region of moderate seismic coupling. Despite the complex foreshock sequence, the main shock rupture was unusually compact for an M_w 8.1 earthquake.

The 2014 Iquique event has demonstrated the effects of rupture details on the directionality of tsunamis. Apart from local resonance associated with the short-period waves, the enhancement of the sidelobe energy to the WNW also contributes to the large wave heights observed in Hawaii. We substantiate the findings with a sensitivity analysis using a simple representation of the earthquake with NNE-SSW and NNW-SSE orientations. The results in Figure S2 for the NNE-SSW orientation show slight underestimation and overestimation of the computed tsunami signals at DART 32402 and 32413 located along and normal to the rupture axis. For the NNW-SSE orientation, the synthetics have interchanged underestimation and overestimation of the recorded data between the two buoys. DART 32401 is located normal to the trench on a symmetric plane of the radiated wavefields from the two sources. The recorded initial waves prior to reflection from the coast are not sensitive to the rupture orientation and cannot be used as constraints for the fault orientation despite the proximity of the station to the source. The radiated wave pattern is confirmed by the amplitude plots in Figure S3 that depict a slightly enhanced side lobe normal to the rupture axis.

The azimuthally well-distributed measurements from DART 32401, 32402, 32412, and 32413 are crucial in constraining the rupture orientation and spatial extent that in turn influence the near- and far-field tsunami. In the absence of DART 32413, the waveform inversion of *An et al.* (2014) yields an elongated slip patch with the long axis in the NNW-SSE. The source would enhance tsunami radiation toward the SSW and underestimate the energy toward Hawaii in the WNW as inferred from Figure S3. In the near field, the southern tip of the rupture is closer to the coast leading to early arrival of the predicted tsunami at Tocopilla by 10 min. NCTR inverted the DART 32401 and 32402 records with a relatively coarse grid of subfaults to provide forecast guidance to the tsunami warning centers. Their results give reasonable agreement with DART and tide gauge records across the Pacific and similar patterns as what our preferred source provides, but with slightly larger tsunami waves toward the Southern Ocean. The underestimation of the initial wave amplitude in Hawaii is likely due to insufficient azimuthal coverage of the DART records in their real-time inversion.

The initial tsunami waveform has a direct relationship with the seafloor deformation even for a compact earthquake source. The subsequent waves from oscillations at the source and the reflection at the coasts are less sensitive to the rupture configuration. The results highlight the need to resolve rupture details to accurately predict near and far-field tsunami impacts from the initial wave. This requires a fine grid of subfaults as well as azimuthally well-distributed DART measurements. The former requires the use of a dispersive wave code to account for attenuation of detailed seafloor excitations over the water column in tsunami generation. The latter is usually not feasible for operations because of the need to provide forecast guidance during the early stage of a tsunami event. Joint inversion with seismic and/or geodetic data sets can supplement the limited coverage from DART buoys to rapidly resolve rupture details for improved tsunami forecasting [*Wei et al.*, 2014]. This holds for larger ruptures with directivity effects as well.

Acknowledgments

The IRIS DMS data center (http://www.iris.edu/hq/) was used to access the seismic data from Global Seismic Network and Federation of Digital Seismic Network stations. The DART and tide gauge data were downloaded from the NOAA National Data Buoy Center (http://www.ndbc.noaa.gov/) and CO-OPS Tsunami Capable Tide Stations (http://tidesandcurrents.noaa.gov/tsunami/). The data analysis made use of GMT, SAC, and Matlab software. We thank Yong Wei and the two anonymous reviewers for their helpful comments. This work was supported by NOAA grant NA09NWS4670016 to Kwok Fai Cheung and by NSF grant EAR1245717 to Thorne Lay. SOEST Contribution Number 9215.

Andrew Newman thanks two anonymous reviewers for their assistance in evaluating this paper.

References

Allgeyer, S., and P. Cummins (2014), Numerical tsunami simulation including elastic loading and seawater density stratification, *Geophys. Res. Lett.*, *41*, 2368–2375, doi:10.1002/2014GL059348.

An, C., I. Sepúlveda, and P. L.-F. Liu (2014), Tsunami source and its validation of the 2014 Iquique, Chile earthquake, *Geophys. Res. Lett.*, *41*, 3988–3994, doi:10.1002/2014GL060567.

Bletery, Q., A. Sladen, B. Delouis, M. Vallée, J.-M. Nocquet, L. Rolland, and J. Jiang (2014), A detailed source model for the M_w 9.0 Tohoku-Oki earthquake reconciling geodesy, seismology and tsunami records, *J. Geophys. Res. Solid Earth*, *119*, doi:10.1002/2014JB011261, in press.

Bretschneider, C. L., H. J. Krock, E. Nakazaki, and F. M. Casciano (1986), Roughness of typical Hawaiian terrain for tsunami run-up calculations: A user's manual, *J.K.K. Look Lab. Rep.*, Univ. of Hawaii, Honolulu.

Brodsky, E. E., and T. Lay (2014), Recognizing foreshocks from the 1 April 2014 Chile earthquake, *Science*, *344*, 700–701, doi:10.1126/science.1255202.

Bürgmann, R. (2014), Warning signs of the Iquique earthquake, *Nature*, doi:10.1038/nature13655.

Cheung, K. F., Y. Bai, and Y. Yamazaki (2013), Surge around the Hawaiian Islands from the 2011 Tohoku tsunami, *J. Geophys. Res. Oceans*, *118*, 5703–5719, doi:10.1002/jgrc.20413.

Comte, D., and M. Pardo (1991), Reappraisal of great historical earthquakes in the northern Chile and southern Peru seismic gaps, *Nat. Hazards*, *4*(1), 23–44, doi:10.1007/BF00126557.

Hayes, G. P., D. J. Wald, and R. L. Johnson (2012), Slab 1.0: A three-dimensional model of global subduction zone geometries, *J. Geophys. Res. 117*, B01302, doi:10.1029/2011JB008524.

Hayes, G. P., M. W. Herman, W. D. Barnhart, K. P. Furlong, S. Riquelme, H. M. Benz, E. Bergman, S. Barrientos, P. S. Earle, and S. Samsonov (2014), Continuing megathrust earthquake potential in Chile after the 2014 Iquique earthquake, *Nature*, doi:10.1038/nature13677.

Kanamori, H., and J. Given (1981), Use of long-period surface waves for rapid determination of earthquake-source parameters, *Phys. Earth Planet. Int.*, *27*, 8–31.

Kanamori, H., and L. Rivera (2008), Source inversion of W phase: Speeding up seismic tsunami warning, *Geophys. J. Int.*, *175*, 222–238.

Kato, A., and S. Nakagawa (2014), Multiple slow-slip events during a foreshock sequence of the 2014 Iquique, Chile M_w 8.1 earthquake, *Geophys. Res. Lett.*, *41*, 5420–5427, doi:10.1002/2014GL061138.

Kikuchi, M., and H. Kanamori (1991), Inversion of complex body waves—III, *Bull. Seismol. Soc. Am.*, *81*(6), 2335–2350.

Lay, T., C. J. Ammon, H. Kanamori, Y. Yamazaki, K. F. Cheung, and A. R. Hutko (2011a), The 25 October 2010 Mentawai tsunami earthquake (M_w 7.8) and the tsunami hazard presented by shallow megathrust ruptures, *Geophys. Res. Lett.*, *38*, L06302, doi:10.1029/2010GL046552.

Lay, T., Y. Yamazaki, C. J. Ammon, K. F. Cheung, and H. Kanamori (2011b), The 2011 M_w 9.0 off the Pacific coast of Tohoku Earthquake: Comparison of deep-water tsunami signals with finite-fault rupture model predictions, *Earth Planets Space*, *63*(7), 797–801, doi:10.5047/eps.2011.05.030.

Lay, T., L. Ye, H. Kanamori, Y. Yamazaki, K. F. Cheung, K. Kwong, and K. D. Koper (2013a), The October 28, 2012 M_w 7.8 Haida Gwaii underthrusting earthquake and tsunami: Slip partitioning along the Queen Charlotte Fault transpressional plate boundary, *Earth Planet. Sci. Lett.*, *375*, 57–70, doi:10.1016/j.epsl.2013.05.005.

Lay, T., L. Ye, H. Kanamori, Y. Yamazaki, K. F. Cheung, and C. J. Ammon (2013b), The February 6, 2013 M_w 8.0 Santa Cruz Islands earthquake and tsunami, *Tectonophysics*, *608*, 1109–1121, doi:10.1016/j.tecto.2013.07.001.

Lay, T., H. Yue, E. E. Brodsky, and C. An (2014), The 1 April 2014 Iquique, Chile, M_w 8.1 earthquake rupture sequence, *Geophys. Res. Lett.*, *41*, 3818–3825, doi:10.1002/2014GL060238.

Lorito, S., F. Romano, S. Atzori, X. Tong, A. Avalione, J. McCloskey, M. Cocco, and A. Piatanesi (2011), Limited overlap between the seismic gap and coseismic slip of the great 2010 Chile earthquake, *Nat. Geosci.*, *4*(3), 173–177, doi:10.1038/ngeo1073.

Okada, Y. (1985), Surface deformation due to shear and tensile faults in a half space, *Bull. Seismol. Soc. Am.*, *75*(4), 1135–1154.

Romano, F., A. Piatanesi, S. Lorito, and K. Hirata (2010), Slip distribution of the 2003 Tokachi-oki M_w 8.1 earthquake from joint inversion of tsunami waveforms and geodetic data, *J. Geophys. Res.*, *115*, B11313, doi:10.1029/2009JB006665.

Romano, F., A. Piatanesi, S. Lorito, N. D'Agostino, K. Hirata, S. Atzori, Y. Yamazaki, and M. Cocco (2012), Clues from joint inversion of tsunami and geodetic data of the 2011 Tohoku-oki earthquake, *Sci. Rep.*, *2*, 385, doi:10.1038/srep00385.

Romano, F., E. Trasatti, S. Lorito, C. Piromallo, A. Piatanesi, Y. Ito, D. Zhao, K. Hirata, P. Lanucara, and M. Cocco (2014), Structural control on the Tohoku earthquake rupture process investigated by 3D FEM, tsunami and geodetic data, *Sci. Rep.*, *4*, 5631, doi:10.1038/srep05631.

Ruiz, S., M. Metois, A. Fuenzalida, J. Ruiz, F. Leyton, R. Grandin, C. Vigny, R. Madariaga, and J. Campos (2014), Intense foreshocks and a slow slip event preceded the 2014 Iquique M_w 8.1 earthquake, *Science*, doi:10.1126/science.1256074.

Saito, T., Y. Ito, D. Inazu, and R. Hino (2011), Tsunami source of the 2011 Tohoku-Oki earthquake, Japan: Inversion analysis based on dispersive tsunami simulations, *Geophys. Res. Lett.*, *38*, L00G19, doi:10.1029/2011GL049089.

Satake, K. (1987), Inversion of tsunami waveforms for the estimation of a fault heterogeneity: Method and numerical experiments, *J. Phys. Earth*, *35*, 241–254.

Satake, K. (1989), Inversion of tsunami waveforms for the estimation of heterogeneous fault moton of large submarine earthquakes: The 1968 Tokachi-Oki and the 198e Japan Sea earthquakes, *J. Geophys. Res.*, *94*, 5627–5636, doi:10.1029/JB094iB05p05627.

Satake, K. (1993), Depth distribution of coseismic slip along the Nankai Trough, Japan from joint inversion of geodetic and tsunami data, *J. Geophys. Res.*, *98*, 4553–4565, doi:10.1029/92JB01553.

Satake, K., et al. (2013), Tsunami source of the 2010 Mentawai, Indonesia earthquake inferred from tsunami field survey and waveform modeling, *Pure Appl. Geophys.*, *1–16*, doi:10.1007/s00024-012-0536-y.

Schurr, B., et al. (2014), Gradual unlocking of plate boundary controlled initiation of the 2014 Iquique earthquake, *Nature*, doi:10.1038/nature13681.

Tanioka, Y., and K. Satake (1996), Tsunami generation by horizontal displacement of ocean bottom, *Geophys. Res. Lett.*, *23*, 861–864, doi:10.1029/96GL00736.

Titov, V. V., F. I. Gonzalez, E. N. Bernard, M. C. Eble, H. O. Mofjeld, J. C. Newman, and A. J. Venturato (2005), Real-time tsunami forecasting: Challenges and solutions, *Nat. Hazards*, *35*(1), 41–58.

Tsai, V. C., J. P. Ampuero, H. Kanamori, and D. J. Stevenson (2013), Estimating the effect of Earth elasticity and variable water density on tsunami speeds, *Geophys. Res. Lett.*, *40*, 492–496, doi:10.1002/grl.50147.

Watada, S., S. Kusumoto, and K. Satake (2014), Traveltime delay and initial phase reversal of distant tsunamis coupled with the self-gravitating elastic Earth, *J. Geophys. Res. Solid Earth*, *119*, 4287–4310, doi:10.1002/2013JB010841.

Wei, Y., K. F. Cheung, G. D. Curtis, and C. S. McCreery (2003), Inversion algorithm for tsunami forecast, *J. Waterw. Port Coast. Ocean Eng.*, *129*(2), 60–69.

Wei, Y., E. N. Bernard, L. Tang, R. Weiss, V. V. Titov, C. Moore, M. Spillane, M. Hopkins, and U. Kânoğlu (2008), Real-time experimental forecast of the Peruvian tsunami of August 2007 for U.S. Coastlines, *Geophys. Res. Lett.*, *35*, L0460, doi:10.1029/2007GL032250.

Wei, Y., A. V. Newman, G. P. Hayes, V. V. Titov, and L. Tang (2014), Tsunami forecast by joint inversion of real-time tsunami waveforms and seismic or GPS data: Application to the Tohoku 2011 tsunami, *Pure Appl. Geophys.*, doi:10.1007/s00024-014-0777-z.

Yagi, Y., R. Okuwaki, B. Enescu, S. Hirano, Y. Yamagami, S. Endo, and T. Komoro (2014), Rupture process of the 2014 Iquique Chile earthquake in relation with the foreshock activity, *Geophys. Res. Lett.*, *41*, 4201–4206, doi:10.1002/2014GL060274.

Yamazaki, Y., and K. F. Cheung (2011), Shelf resonance and impact of near-field tsunami generated by the 2010 Chile earthquake, *Geophys. Res. Lett.*, *38*, L12605, doi:10.1029/2011GL047508.

Yamazaki, Y., Z. Kowalik, and K. F. Cheung (2009), Depth-integrated, non-hydrostatic model for wave breaking and run-up, *Int. J. Numer. Meth. Fluid.*, *61*(5), 473–497.

Yamazaki, Y., K. F. Cheung, and Z. Kowalik (2011a), Depth-integrated, non-hydrostatic model with grid nesting for tsunami generation, propagation, and run-up, *Int. J. Numer. Meth. Fluid.*, *67*(12), 2081–2107.

Yamazaki, Y., T. Lay, K. F. Cheung, H. Yue, and H. Kanamori (2011b), Modeling regional and remote tsunami observations with finite-fault slip models for the 11 March 2011 Tohoku earthquake (M_w 9.0), *Geophys. Res. Lett.*, *38*, L00G15, doi:10.1029/2011GL049130.

Yamazaki, Y., K. F. Cheung, G. Pawlak, and T. Lay (2012), Surges along the Honolulu coast from the 2011 Tohoku tsunami, *Geophys. Res. Lett.*, *39*, L09604, doi:10.1029/2012GL051624.

Yamazaki, Y., K. F. Cheung, and T. Lay (2013), Generation mechanism and near-field dynamics of the 2011 Tohoku tsunami, *Bull. Seismol. Soc. Am.*, *103*, 1444–1455, doi:10.1785/0120120103.

Yokota, Y., K. Koketsu, Y. Fujii, K. Satake, S. Sakai, M. Shinohara, and T. Kanazawa (2011), Joint inversion of strong motion, teleseismic, geodetic and tsunami datasets for the rupture process of the 2011 Tohoku earthquake, *Geophys. Res. Lett.*, *38*, L00G21, doi:10.1029/2011GL050098.

Yue, H., T. Lay, L. Rivera, Y. Bai, Y. Yamazaki, K. F. Cheung, E. M. Hill, K. Sieh, W. Kongko, and A. Muhari (2014a), Rupture process of the 2010 M_w 7.8 Mentawai tsunami earthquake from joint inversion of near-field hr-GPS and teleseismic body wave recordings constrained by tsunami observations, *J. Geophys. Res. Solid Earth*, *119*, 5574–5593, doi:10.1002/2014JB011082.

Yue, H., T. Lay, L. Rivera, C. An, C. Vigny, and X. Tong (2014b), Localized fault slip to the trench in the 2010 Maule, Chile M_w 8.8 earthquake from joint inversion of high-rate GPS, teleseismic body waves, InSAR and tsunami observations, *J. Geophys. Res. Solid Earth*, *119*, doi:10.1002/2014JB011340.

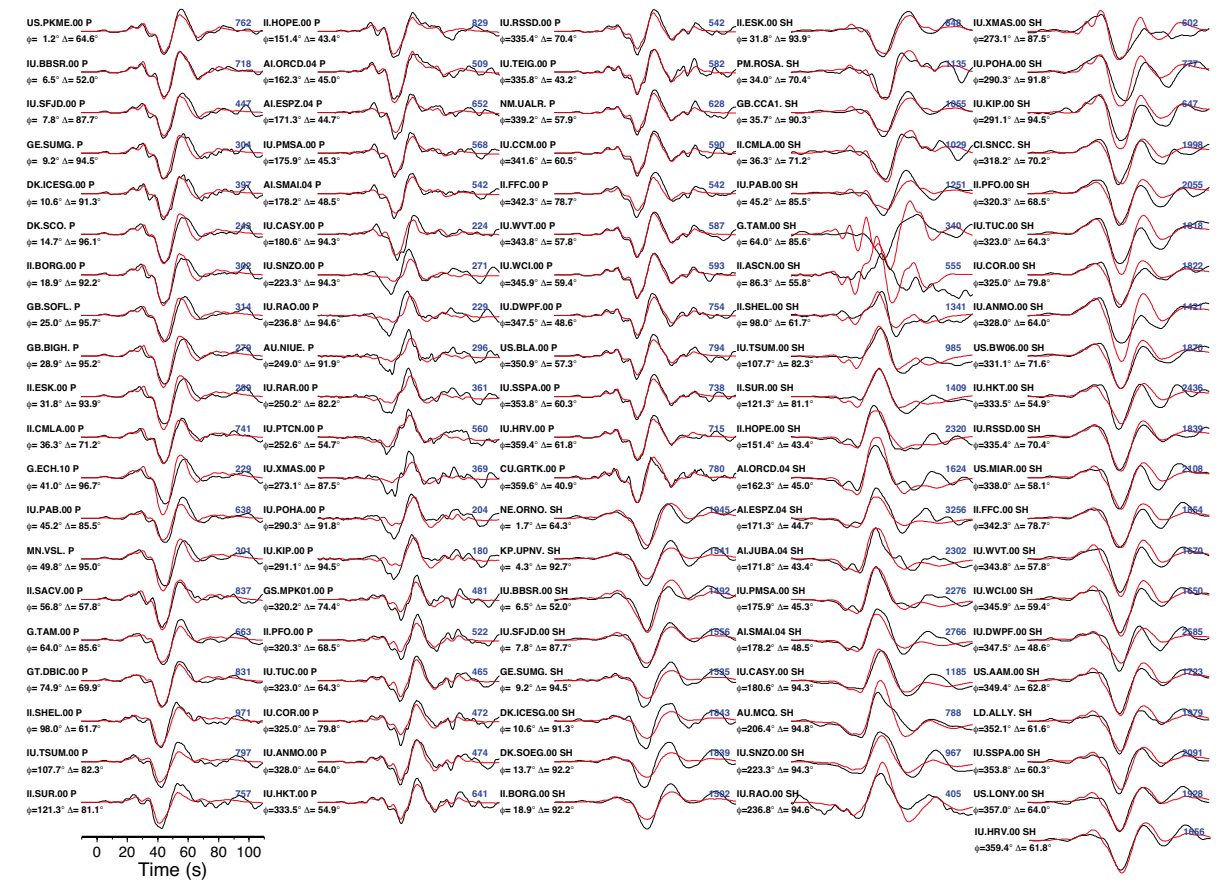
US.PKME.00 P
ϕ= 1.2° Δ= 64.6°
762
II.HOPE.00 P
ϕ=151.4° Δ= 43.4°
829
IU.RSSD.00 P
ϕ=335.4° Δ= 70.4°
542
II.ESK.00 SH
ϕ= 31.8° Δ= 93.9°
603
IU.XMAS.00 SH
ϕ=273.1° Δ= 87.5°
602
IU.BBSR.00 P
ϕ= 6.5° Δ= 52.0°
718
AI.ORCD.04 P
ϕ=162.3° Δ= 45.0°
509
IU.TEIG.00 P
ϕ=335.8° Δ= 43.2°
582
PM.ROSA. SH
ϕ= 34.0° Δ= 70.4°
1135
IU.POHA.00 SH
ϕ=290.3° Δ= 91.8°
721
IU.SFJD.00 P
ϕ= 7.8° Δ= 87.7°
447
AI.ESPZ.04 P
ϕ=171.3° Δ= 44.7°
652
NM.UALR. P
ϕ=339.2° Δ= 57.9°
628
GB.CCA1. SH
ϕ= 35.7° Δ= 90.3°
1955
IU.KIP.00 SH
ϕ=291.1° Δ= 94.5°
647
GE.SUMG. P
ϕ= 9.2° Δ= 94.5°
304
IU.PMSA.00 P
ϕ=175.9° Δ= 45.3°
568
II.CCM.00 P
ϕ=341.6° Δ= 60.5°
590
II.CMLA.00 SH
ϕ= 36.3° Δ= 71.2°
1029
CI.SNCC. SH
ϕ=318.2° Δ= 70.2°
1998
DK.ICESG.00 P
ϕ= 10.6° Δ= 91.3°
397
AI.SMAI.04 P
ϕ=178.2° Δ= 48.5°
542
II.FFC.00 P
ϕ=342.3° Δ= 78.7°
542
IU.PAB.00 SH
ϕ= 45.2° Δ= 85.5°
1251
II.PFO.00 SH
ϕ=320.3° Δ= 68.5°
2055
DK.SCO. P
ϕ= 14.7° Δ= 96.1°
249
IU.CASY.00 P
ϕ=180.6° Δ= 94.3°
224
IU.WVT.00 P
ϕ=343.8° Δ= 57.8°
587
G.TAM.00 SH
ϕ= 64.0° Δ= 85.6°
340
IU.TUC.00 SH
ϕ=323.0° Δ= 64.3°
1618
II.BORG.00 P
ϕ= 18.9° Δ= 92.2°
390
IU.SNZO.00 P
ϕ=223.3° Δ= 94.3°
271
IU.WCI.00 P
ϕ=345.9° Δ= 59.4°
593
II.ASCN.00 SH
ϕ= 86.3° Δ= 55.8°
555
IU.COR.00 SH
ϕ=325.0° Δ= 79.8°
1822
GB.SOFL. P
ϕ= 25.0° Δ= 95.7°
314
IU.RAO.00 P
ϕ=236.8° Δ= 94.6°
229
IU.DWPF.00 P
ϕ=347.5° Δ= 48.6°
754
II.SHEL.00 SH
ϕ= 98.0° Δ= 61.7°
1341
IU.ANMO.00 SH
ϕ=328.0° Δ= 64.0°
1421
GB.BIGH. P
ϕ= 28.9° Δ= 95.2°
279
AU.NIUE. P
ϕ=249.0° Δ= 91.9°
296
US.BLA.00 P
ϕ=350.9° Δ= 57.3°
794
IU.TSUM.00 SH
ϕ=107.7° Δ= 82.3°
985
US.BW06.00 SH
ϕ=331.1° Δ= 71.6°
1826
II.ESK.00 P
ϕ= 31.8° Δ= 93.9°
289
IU.RAR.00 P
ϕ=250.2° Δ= 82.2°
361
IU.SSPA.00 P
ϕ=353.8° Δ= 60.3°
738
II.SUR.00 SH
ϕ=121.3° Δ= 81.1°
1409
IU.HKT.00 SH
ϕ=333.5° Δ= 54.9°
2436
II.CMLA.00 P
ϕ= 36.3° Δ= 71.2°
741
IU.PTCN.00 P
ϕ=252.6° Δ= 54.7°
560
IU.HRV.00 P
ϕ=359.4° Δ= 61.8°
715
II.HOPE.00 SH
ϕ=151.4° Δ= 43.4°
2320
IU.RSSD.00 SH
ϕ=335.4° Δ= 70.4°
1839
G.ECH.10 P
ϕ= 41.0° Δ= 96.7°
229
IU.XMAS.00 P
ϕ=273.1° Δ= 87.5°
369
CU.GRTK.00 P
ϕ=359.6° Δ= 40.9°
780
AI.ORCD.04 SH
ϕ=162.3° Δ= 45.0°
1624
US.MIAR.00 SH
ϕ=338.0° Δ= 58.1°
2108
IU.PAB.00 P
ϕ= 45.2° Δ= 85.5°
638
IU.POHA.00 P
ϕ=290.3° Δ= 91.8°
204
NE.ORNO. SH
ϕ= 1.7° Δ= 64.3°
1945
AI.ESPZ.04 SH
ϕ=171.3° Δ= 44.7°
3256
II.FFC.00 SH
ϕ=342.3° Δ= 78.7°
1864
MN.VSL. P
ϕ= 49.8° Δ= 95.0°
301
IU.KIP.00 P
ϕ=291.1° Δ= 94.5°
180
KP.UPNV. SH
ϕ= 4.3° Δ= 92.7°
1541
AI.JUBA.04 SH
ϕ=171.8° Δ= 43.4°
2302
IU.WVT.00 SH
ϕ=343.8° Δ= 57.8°
1870
II.SACV.00 P
ϕ= 56.8° Δ= 57.8°
837
GS.MPK01.00 P
ϕ=320.2° Δ= 74.4°
481
IU.BBSR.00 SH
ϕ= 6.5° Δ= 52.0°
1102
IU.PMSA.00 SH
ϕ=175.9° Δ= 45.3°
2276
IU.WCI.00 SH
ϕ=345.9° Δ= 59.4°
1650
G.TAM.00 P
ϕ= 64.0° Δ= 85.6°
583
II.PFO.00 P
ϕ=320.3° Δ= 68.5°
522
IU.SFJD.00 SH
ϕ= 7.8° Δ= 87.7°
1556
AI.SMAI.04 SH
ϕ=178.2° Δ= 48.5°
2766
IU.DWPF.00 SH
ϕ=347.5° Δ= 48.6°
2685
GT.DBIC.00 P
ϕ= 74.9° Δ= 69.9°
831
IU.TUC.00 P
ϕ=323.0° Δ= 64.3°
465
GE.SUMG. SH
ϕ= 9.2° Δ= 94.5°
1335
IU.CASY.00 SH
ϕ=180.6° Δ= 94.3°
1185
US.AAM.00 SH
ϕ=349.4° Δ= 62.8°
1793
II.SHEL.00 P
ϕ= 98.0° Δ= 61.7°
971
IU.COR.00 P
ϕ=325.0° Δ= 79.8°
472
DK.ICESG.00 SH
ϕ= 10.6° Δ= 91.3°
1843
AU.MCQ. SH
ϕ=206.4° Δ= 94.8°
788
LD.ALLY. SH
ϕ=352.1° Δ= 61.6°
1879
IU.TSUM.00 P
ϕ=107.7° Δ= 82.3°
797
IU.ANMO.00 P
ϕ=328.0° Δ= 64.0°
474
DK.SOEG.00 SH
ϕ= 13.7° Δ= 92.2°
1809
IU.SNZO.00 SH
ϕ=223.3° Δ= 94.3°
967
IU.SSPA.00 SH
ϕ=353.8° Δ= 60.3°
2091
II.SUR.00 P
ϕ=121.3° Δ= 81.1°
757
IU.HKT.00 P
ϕ=333.5° Δ= 54.9°
641
II.BORG.00 SH
ϕ= 18.9° Δ= 92.2°
1982
IU.RAO.00 SH
ϕ=236.8° Δ= 94.6°
405
US.LONY.00 SH
ϕ=357.0° Δ= 64.0°
1928
IU.HRV.00 SH
ϕ=359.4° Δ= 61.8°
1866
0 20 40 60 80 100
Time (s)

Case 1 NNE-SSW

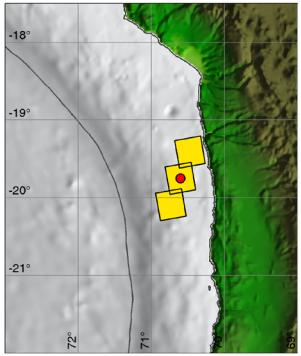

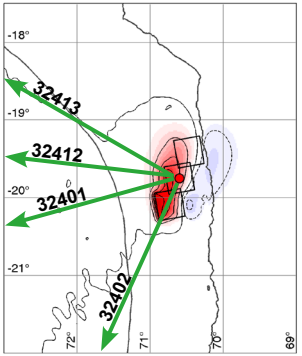

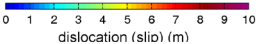

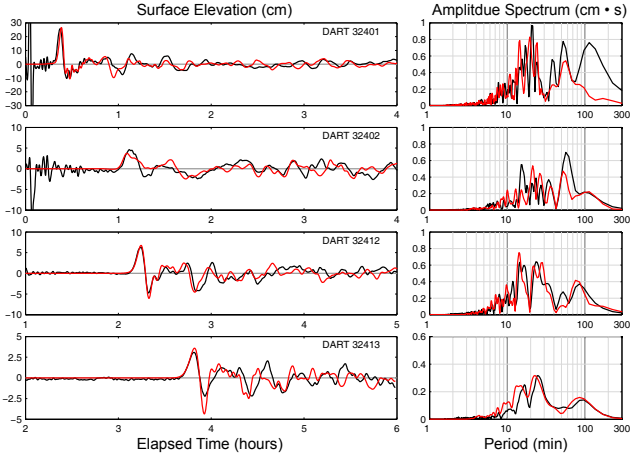

Case 2 NNW-SSE

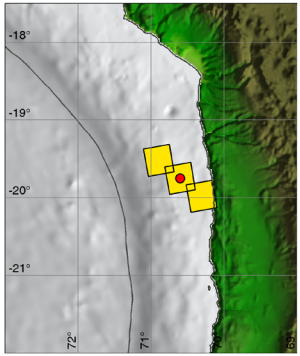

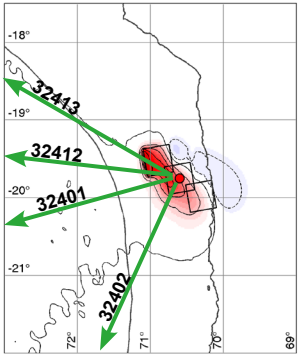

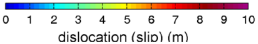

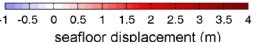

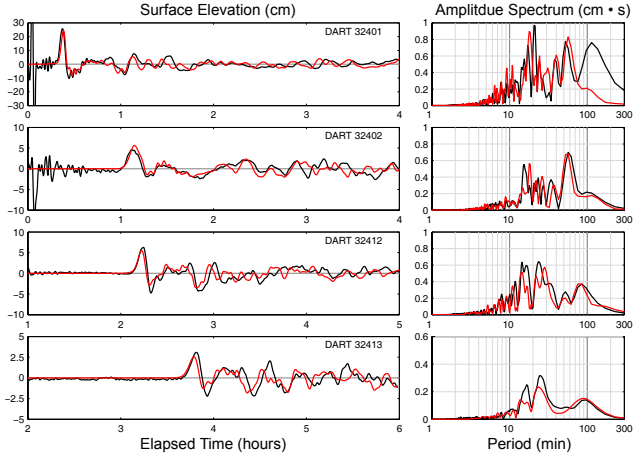

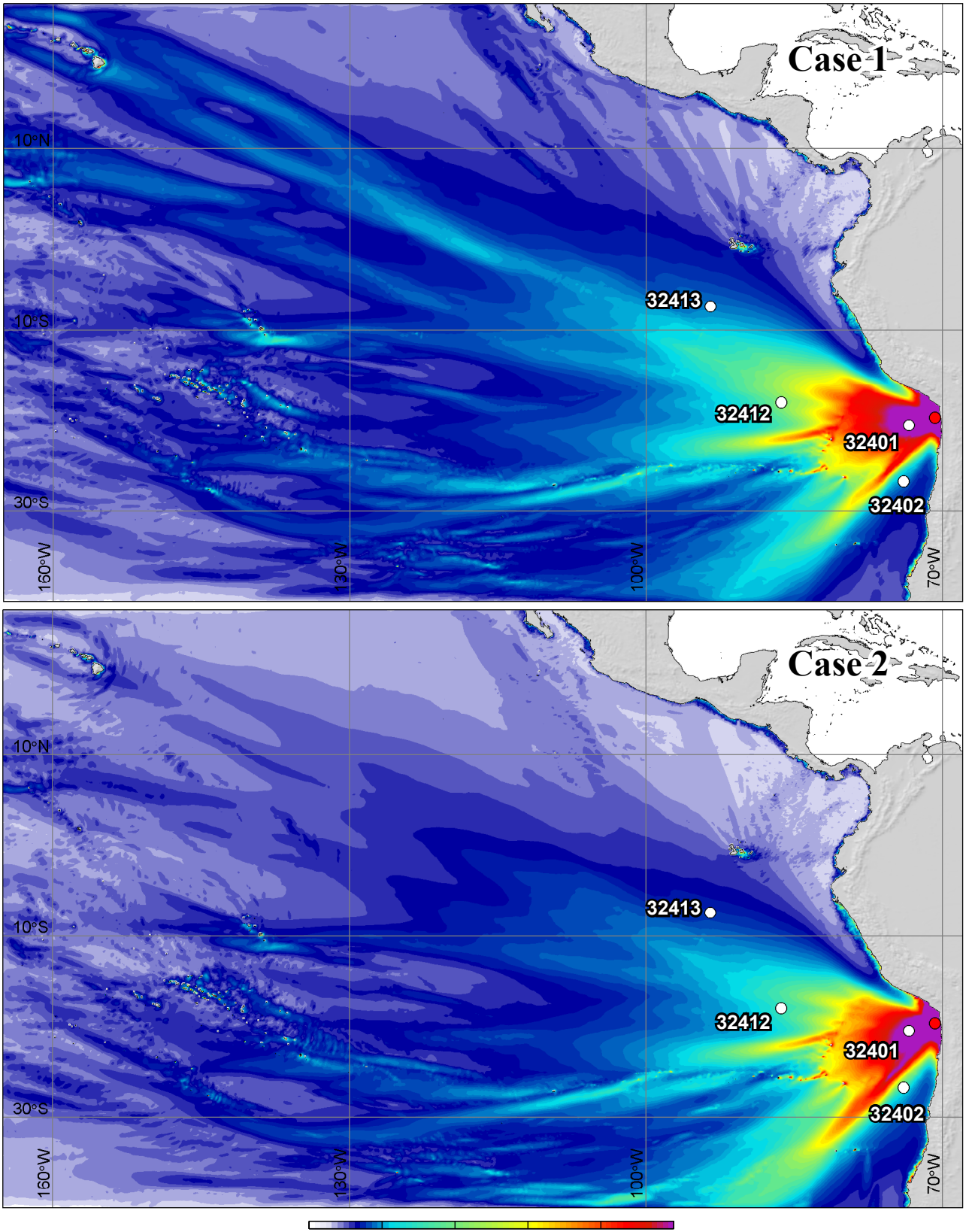
Case 1
10°N
10°S
30°S
160°W
130°W
100°W
70°W
32413
32412
32401
32402
Case 2
10°N
10°S
30°S
160°W
130°W
100°W
70°W
32413
32412
32401
32402
0
0.04
0.08
0.12
0.16
0.2 + m